Article

Antarctic extreme seasons under 20th and 21st century climate change

Check for updates

Thomas J. Bracegirdle [1] ✉, **Thomas Caton Harrison**[1], **Caroline R. Holmes**[1], **Hua Lu**[1],
Patrick Martineau [2] & **Tony Phillips** [1]

In this study, available large ensemble datasets in the Coupled Model Intercomparison Phase 6 (CMIP6) archive were used to provide the first multi-variate overview of the evolution of extreme seasons over Antarctica and the Southern Ocean during the 20th and 21st centuries following medium-to-high radiative forcing scenarios. The results show significant differences between simulated changes in background mean climate and changes in low (10th percentile) and high (90th percentile) extreme seasons. Regional winter warming is most pronounced for cold extremes. In summer, there are more pronounced increases in high extremes in precipitation and westerly wind during the ozone hole formation period (late 20th century), affecting coastal regions and, in particular, the Antarctic Peninsula. At midlatitudes, there is a reduction in the range of summer season wind extremes. Suggested mechanisms for these differences are provided relating to sea ice retreat and westerly jet position.

Projected 21st-century changes in climate over Antarctica and the Southern Ocean are expected to have major impacts on physical and biological systems, with profound implications globally[1]. Extensive research has been conducted on the time-mean Antarctic climate responses to external drivers such as changing greenhouse gas concentrations and stratospheric ozone depletion and recovery[2,3]. However, a comprehensive assessment of variability and extreme weather and climate events is of greater importance in terms of impacts. Extreme seasons (which are classed as climate extremes within the Intergovernmental Panel on Climate Change (IPCC) Sixth Assessment AR6 report) are of particular relevance as they can produce accumulated effects of greater impact than a single weather event. For example, the breakup of the Larsen B Ice Shelf occurred following a summer of persistent surface melt in 2002[4]. Extreme events already drive increased surface melting on other floating ice shelves[5] with the potential to accelerate retreat, thinning and even break-up. This leads to the grounded ice streams flowing into the ocean faster and thus contributing to global sea level rise[6]. From an ecosystem perspective, penguin breeding can be severely affected by persistent adverse conditions over a season[7]. Key atmospheric variables in terms of impacts of extremes in Antarctica include near-surface temperature, precipitation and near-surface wind[8]. There is a gap in knowledge on how extreme seasons may change over Antarctica and the Southern Ocean under future climate forcing scenarios, with Antarctica not included in the IPCC AR6 WG1 Chapter 11 on extremes[9]. One reason for this is that a rigorous assessment of the behaviour of extreme conditions requires a large number of climate model simulations, or 'large ensembles' (LEs), which are only now becoming widely available.

Projected changes in seasonal extremes will not necessarily follow changes in the climate mean state[10]. For example, sea ice is known to significantly influence the year-to-year variability of surface air temperature, both over the ice itself and over adjacent land and ice shelves[11], and affect seasonal temperature and precipitation extremes in Arctic climate projections[12,13]. This is because surface air temperatures over open oceans are unable to reach the very low values that are possible over frozen ice/snow. This effect is seen in the observational records over the Antarctic Peninsula, in particular at Vernadsky station (in the northwest region of the Antarctic Peninsula), where observed warming trends are associated with a loss of cold extremes caused by an increased occurrence of ice-free conditions over the adjacent ocean[14,15]. At lower latitudes, decreases in meridional temperature gradient associated with polar amplification are a factor in reducing synoptic temperature variability under climate change[10,16], which may have implications for the seasonal timescale. Another aspect of the climate system of relevance to extreme conditions is the Southern Hemisphere mid-latitude tropospheric westerly jet (and the associated storm track), which exhibits changes in time-mean latitude and speed under climate forcing. Specifically, there is a poleward shift and strengthening under greenhouse gas increases year-round and in response to stratospheric ozone depletion in summer, along with associated changes in variability and increases in precipitation at high latitudes as the mid-latitude storm track moves poleward with the jet[17–19]. Although the jet variability occurs predominantly on weekly timescales, the occurrence of extreme wind events exhibits a close association with seasonal mean wind[20]. Extreme seasons in wind and related variables could, therefore, be altered by such changes in jet

[1]British Antarctic Survey, Cambridge, UK. [2]Japan Agency for Marine–Earth Science and Technology, Yokohama, Japan. ✉e-mail: tjbra@bas.ac.uk

structure, for example, as poleward shifts of the jet encroach on new locations on its poleward flank, which straddles the Antarctic Peninsula.

In this paper, we use available LE output from the Coupled Model Intercomparison Project Phase 6 (CMIP6) dataset[21] to provide a broad overview of extreme seasons under climate change for near-surface temperature, precipitation and near-surface westerly winds over Antarctica and the Southern Ocean. Here, extreme seasons are defined relative to background climate as it evolves in time, rather than by fixed thresholds (see the "Methods" section for details). This approach provides a picture of the relative change of extreme seasons over time across a range of locations and variables. Here we aim to address the following questions:

- How will extreme warm and cold seasons evolve into the future, especially in regions of retreating sea ice?
- How will the projected poleward shift and strengthening of circumpolar tropospheric westerlies influence changes in seasonal extremes?

Answering such questions provides an important context for future more detailed impact-specific studies and addresses a gap in communicating the potential range of future conditions associated with both changes in background time-mean (e.g. 30-year) climate conditions and changes in seasonal extremes.

Results

Surface air temperature

Figure 1 shows winter (June–August; JJA) surface air temperature (TAS) at two time slices, pre ozone hole (1960) and late 21st century (2080), and the differences between them (2080–1960). It shows multi-model mean diagnostics from historical and SSP3-7.0 scenario simulations of the CMIP6 models. Both background climate and high and low extremes are shown (see the "Methods" section for full definitions of the notation, the calculations conducted and details of the CMIP6 LE output used). Changes in background climate (Fig. 1j) exhibit the well-established pattern of strongest warming over regions of sea ice retreat[22,23]. This is due to the large atmosphere–ocean temperature differences and resulting large anomalous fluxes of heat and moisture over newly exposed ice-free ocean[14]. Patterns of change in extreme indices qualitatively show a similar pattern to the
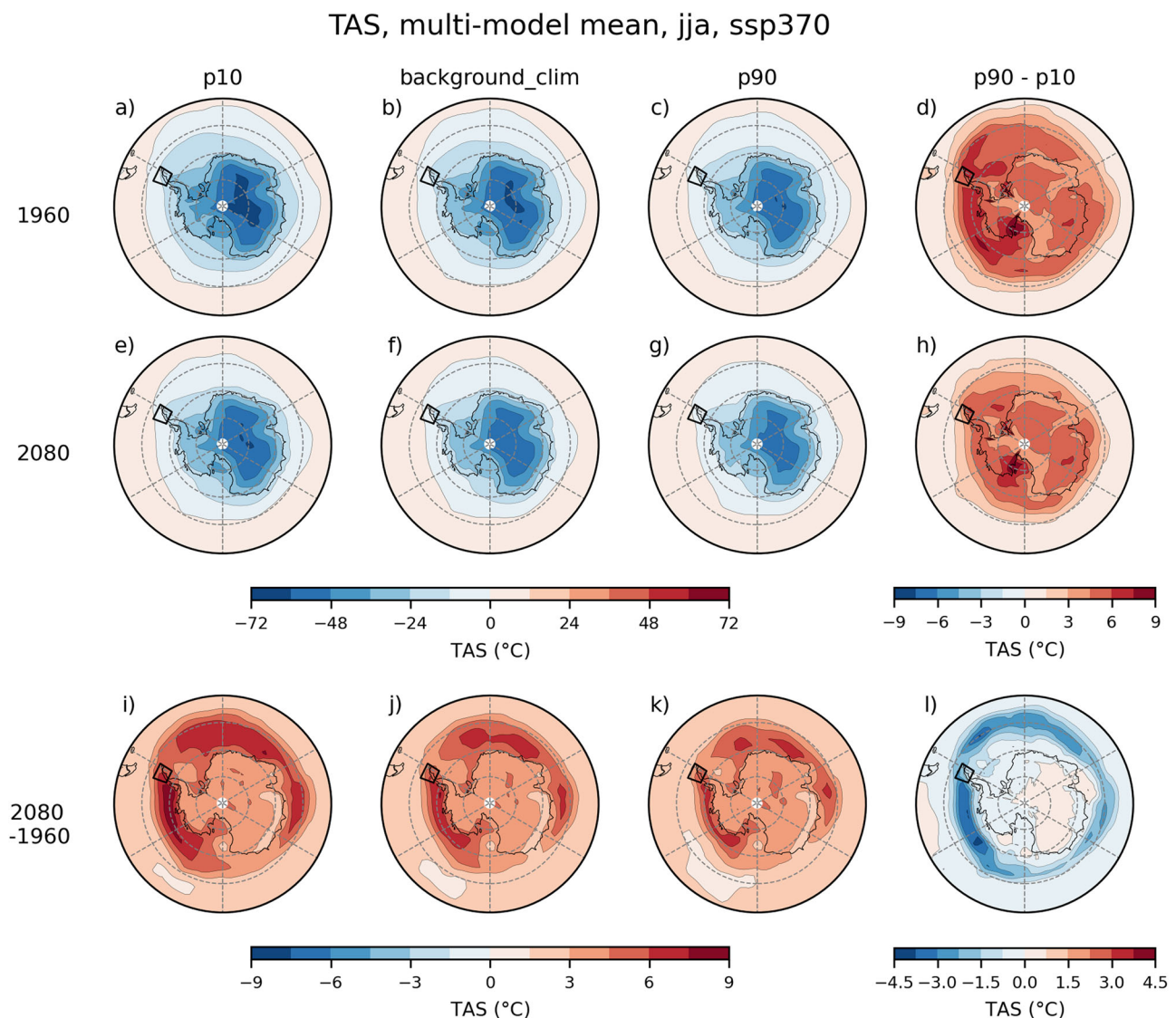
Fig. 1 | CMIP6 multi-model mean winter (JJA) surface-air temperature (TAS) climatologies both pre-ozone hole (1960, from historical runs, top row) and late 21st century (2080, from SSP3-7.0 runs, middle row) and difference between 2080 and 1960 (bottom row). The columns show, from left to right, cold extremes (p10) (**a, e, i**), background mean climate (background_clim) (**b, f, j**), warm extremes (p90) (**c, g, k**) and the differences between warm and cold extremes (i.e. the 3rd column minus the first column) (**d, h, l**). The box with bold black borders shows the location of the north Peninsula region referred to in the main text and used in time series plots in Fig. 4. The box spans the latitudes 62.5°S–67.5°S and longitudes 70°W–57.5°W.
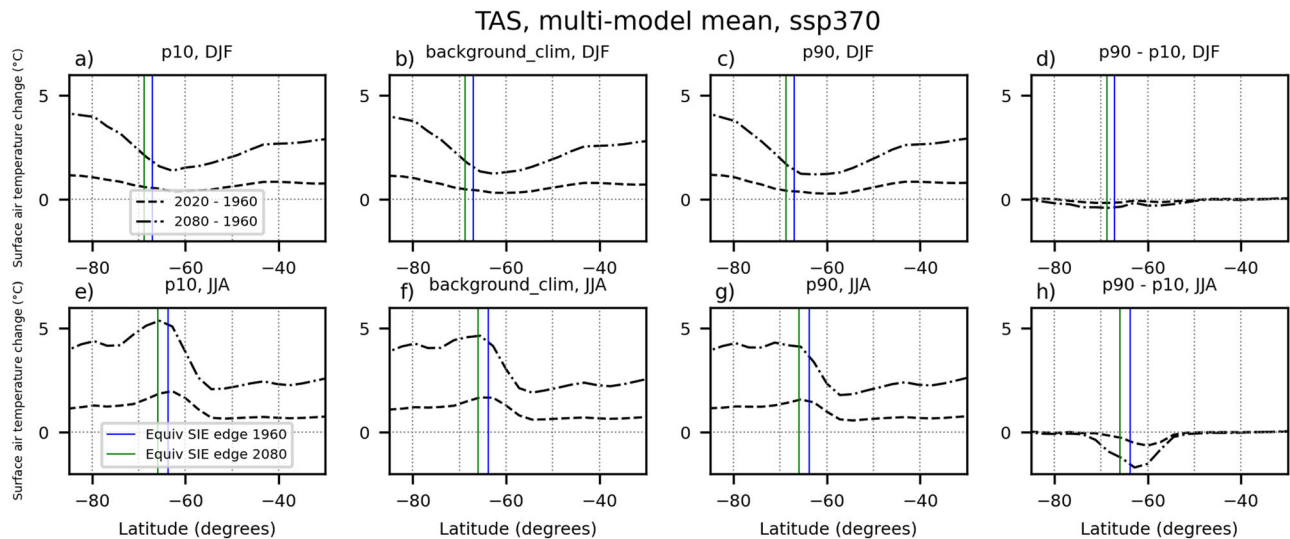
Fig. 2 | CMIP6 multi-model mean zonal mean summer (upper row) and winter (lower row) TAS changes in 2020 and 2080 relative to 1960 (pre-ozone hole). Changes are shown for low extremes (p10) (left column, **a**, **e**), background climate (second column, **b**, **f**), high extremes (**c**, **g**) and the differences between p90 and p10 (right column, **d**, **h**). Climatologies of the multi-model mean equivalent latitudes (see Methods) of the sea ice edge are shown, centred on the years 1960 (blue vertical lines) and 2080 (green vertical lines).

background climate response, with the strongest warming over newly exposed ice-free ocean. However, comparing Fig. 1i and k it is evident that changes in cold extremes (TAS_{p10}) are larger and more extensive than changes in warm extremes (TAS_{p90}) over regions of retreating sea ice. This behaviour extends to adjacent coastal margins, in particular over the northern Antarctic Peninsula and emerges in zonal averages (Fig. 2e–h). The zonal averages also demonstrate that at most latitudes shown there is very little difference between changes in high and low extremes (Fig. 2h). It is only over the sea ice zone that such large differences emerge (as large as 1.74 °C in magnitude at 63°S in Fig. 2h). Appealing to output from different individual climate models with different amounts of simulated historical sea ice provides further evidence for the role of sea ice. The UKESM1-0-LL model exhibits clear sea ice retreat and pronounced p90–p10 differences in the vicinity of the model-simulated sea ice edge in winter (Fig. 3). In contrast, the MIROC6 model has very little sea ice, even in winter, and shows only negligible differences between 21st-century changes in high (p90) and low (p10) extreme winters (Fig. S1). The edge of the sea ice marks a transition from an open ocean marine regime of small p90–p10 and a regime of large p90–p10 at almost all locations poleward of the sea ice edge (both over sea ice and over land). There is an additional factor along the sea ice edge of variability in sea ice itself, which is largest along the sea ice edge (example shown in Fig. S2). This provides an additional driver of year-to-year variability in winter temperature and particularly large p90–p10 in TAS exceeding those over regions of consistent winter sea ice cover and the Antarctic continent.

To examine change over the northern Antarctic Peninsula coastal margin in more detail, Fig. 4a, b shows time series plots for a region over the northern Antarctic Peninsula, which includes Vernadsky research base and the Larsen ice shelves (region indicated in Fig. 1). In winter the cold extremes (TAS_{p10}) exhibit more pronounced warming than warm extremes (TAS_{p90}) over the 21st century (Fig. 4b) (5.6 °C compared to 4.4 °C between 1960 and 2080), which is consistent with the observed link between temperature and variability of adjacent sea ice in the region[14,15].

For summer (DJF), the strongest late-century warming is projected to occur over the interior of the Antarctic continent (Fig. 2b) and over the major ice shelves (Ross and Filchner-Ronne) (Fig. S3). Unlike in winter, projected zonally-averaged warming in extreme summers closely follows background climate change, i.e., TAS_{p10}, $TAS_{background\_clim}$ and TAS_{p90} exhibit very similar changes (Fig. 2a–c). Two key explanations for this are (i)

in summer, the sea surface is not significantly warmer than the atmosphere, and therefore areas of open ocean newly exposed by sea ice retreat do not have a significant warming influence on the atmosphere and (ii) the smaller sea ice extent in summer (e.g. ref. 24). Time series of summer warming over the northern Peninsula does, however, highlight that, although summer warming is weaker than in winter, the range between TAS_{p90} and TAS_{p10} is also smaller (i.e. smaller internal variability) (Fig. 4a, b). An implication of this is that projected changes in the summer, although being smaller in magnitude, still shift conditions away from their historical range by a similar amount (or even slightly more) than in winter.

Near-surface westerly wind

Spatial maps of background change in summer near-surface zonal wind (UAS) exhibit well-established patterns of change through the 20th and 21st century associated with strengthening and poleward shifting of the circumpolar westerlies, and associated weakening of coastal easterlies, following the SSP3-7.0 forcing scenario (Fig. 5b, f, j)[25,26]. Time series at example locations shown in Fig. 4c, e (the northern Peninsula box was chosen due to its importance for impacts on Peninsula ice shelves and because long-term observations have shown past links between winter temperature and sea ice variability and the S Ocean box was picked as an example location with a large decrease in UAS_{p90}–UAS_{p10}) highlight the importance of stratospheric ozone depletion for summer trends in the late 20th century (e.g. ref. 27). Specifically, there is a period of increasing summer westerlies that is particularly pronounced during the decade of the 1980s.

In terms of extreme seasons, multi-model mean changes in summer broadly follow the background climate change with poleward shifting and strengthening evident in zonal mean p10 and p90 (Fig. 6, top row). On the poleward side of the climatological jet, there is a region of strong year-to-year variability that manifests as a peak in UAS_{p90}–UAS_{p10} at about 60°S (Fig. 6d). This shifts poleward with the time-mean jet under forcing, resulting in a reduction in variability between 55 and 60°S (i.e. a reduction in UAS_{p90}–UAS_{p10} of up to 1.2 m s^{-1} in magnitude in Fig. 6d). On the poleward side of this maximum in p90–p10 (~60–65°S) there is no accompanying clear increase in variability.

The zonal mean results are reflected in the time series over the northern Peninsula region, where evolutions in the extremes and background climate of summer-mean UAS broadly follow each other (Fig. 4c). At mid-latitudes, at a location chosen to sample the region of clearest difference in Fig. 5l
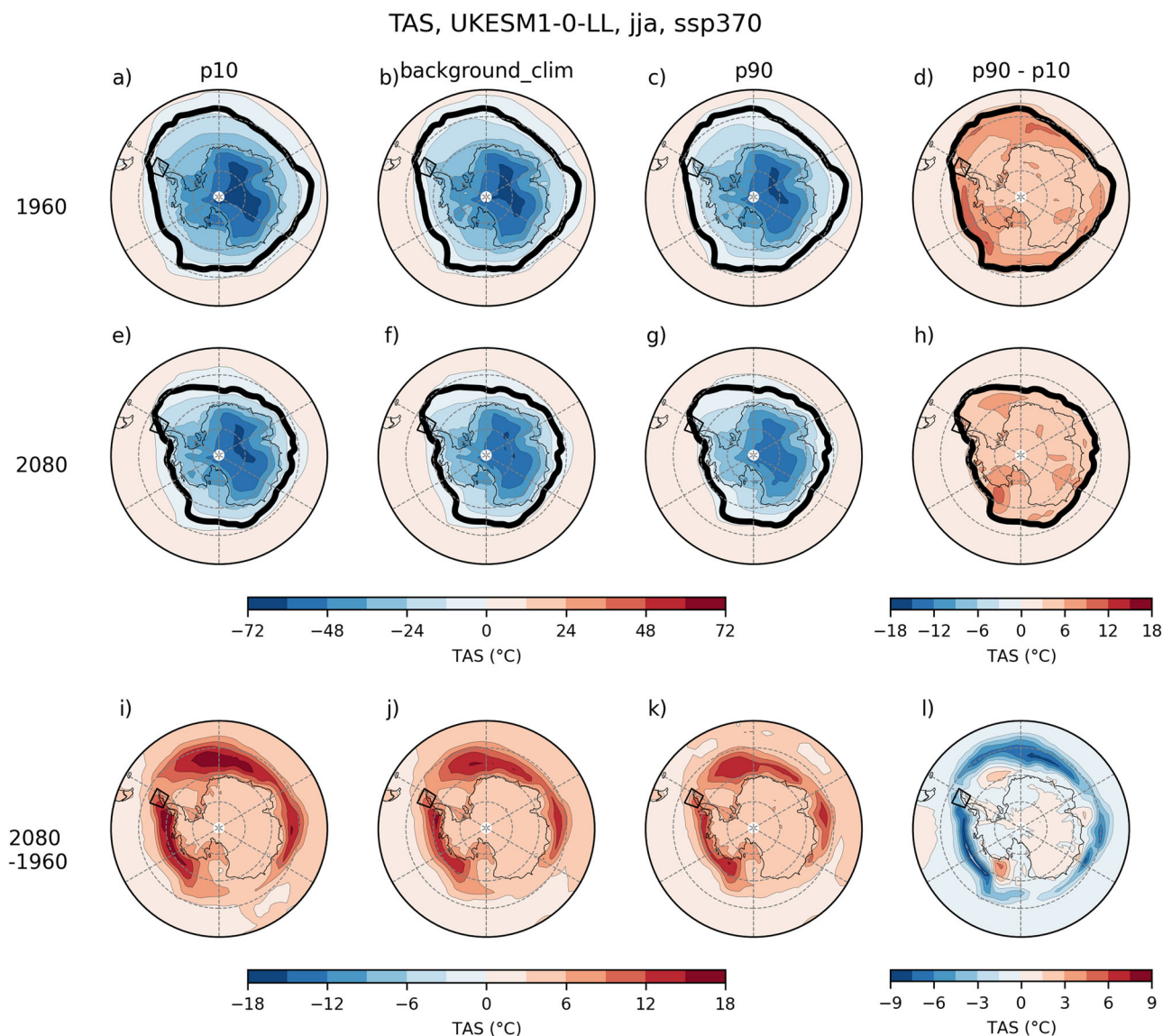
Fig. 3 | Winter (JJA) surface-air temperature (TAS) climatologies for both pre-ozone hole (1960) and late 21st century (2080) and differences between 2080 and 1960. As in Fig. 1, but for just the UKESM1-0-LL model and with the 15% contour of climatological winter (JJA) sea ice concentration added to (**a–h**; bold black line). Note that different colour scales to Fig. 1 are used in the difference plots (**d**, **h–l**).

(lower right panel—location indicated by box with dashed border), the stronger increase in p10 (2 m s⁻¹ between 1960 and 2080), compared to the background climate (1.44 m s⁻¹) and p90 (0.75 m s⁻¹), occurs through the late 20th century ozone depletion period and the 21st century (Fig. 4e). The zonal 10 m wind time series extracted for the same regions from ERA5 exhibit similar ranges of variability as produced in the models. It is, however, difficult to compare ensemble mean trends from model simulations with the single realisation of the observed climate due to the influence of internal climate variability.

For winter (JJA) (Fig. 6, lower row), the time mean jet structure is very different from summer, appearing much more latitudinally diffuse in the zonal mean. This is in part due to zonal asymmetries, in particular a split of the jet into two branches between Australia and New Zealand, and also due to the presence of the winter sub-tropical jet (e.g. refs. 28,29). The associated structures in UAS$_{p90}$, UAS$_{p10}$, and their range (i.e. p90–p10) also exhibit weak meridional gradients (Fig. 6e, g, h). This helps explain why poleward shifts in the jet have only a small effect on the range between high and low extremes (i.e. variability in winter-mean winds), with changes in extreme seasons approximately mirroring changes in background climate (Fig. 6h). It is notable that the winter season winds show no evidence of the

preferential influence of sea ice decline on proximal high and low extremes that is seen for surface air temperature (Fig. 2h). However, this may be expected as known mechanisms for the response of the jet to a range of forcing factors, including sea ice and ocean surface change, generally involve non-local dynamics involving mid-latitude eddy momentum transport[29–32]. Effects related to changes in surface friction as open ocean replaces sea ice appear too small to emerge as significant in the models assessed. Time series plots from high (Fig. 4d) and mid (Fig. 4f) latitudes show a gradual emergence of increasing westerlies through the 21st century. The time series from ERA5 are consistent with the climate model results, with little indication of an overall trend in the modern satellite era.

Precipitation

Background changes in summer (DJF) precipitation following historical and SSP3-7.0 forcing exhibit broadscale 21st-century increases over the Southern Ocean and large, more regional, increases over parts of coastal Antarctica, in particular over the western part of the Antarctic Peninsula (Fig. 7j).

At almost all locations over mid-high southern latitudes, changes in high extreme, 'wet', seasons (PR$_{p90}$) are larger than for low extremes (PR$_{p10}$)
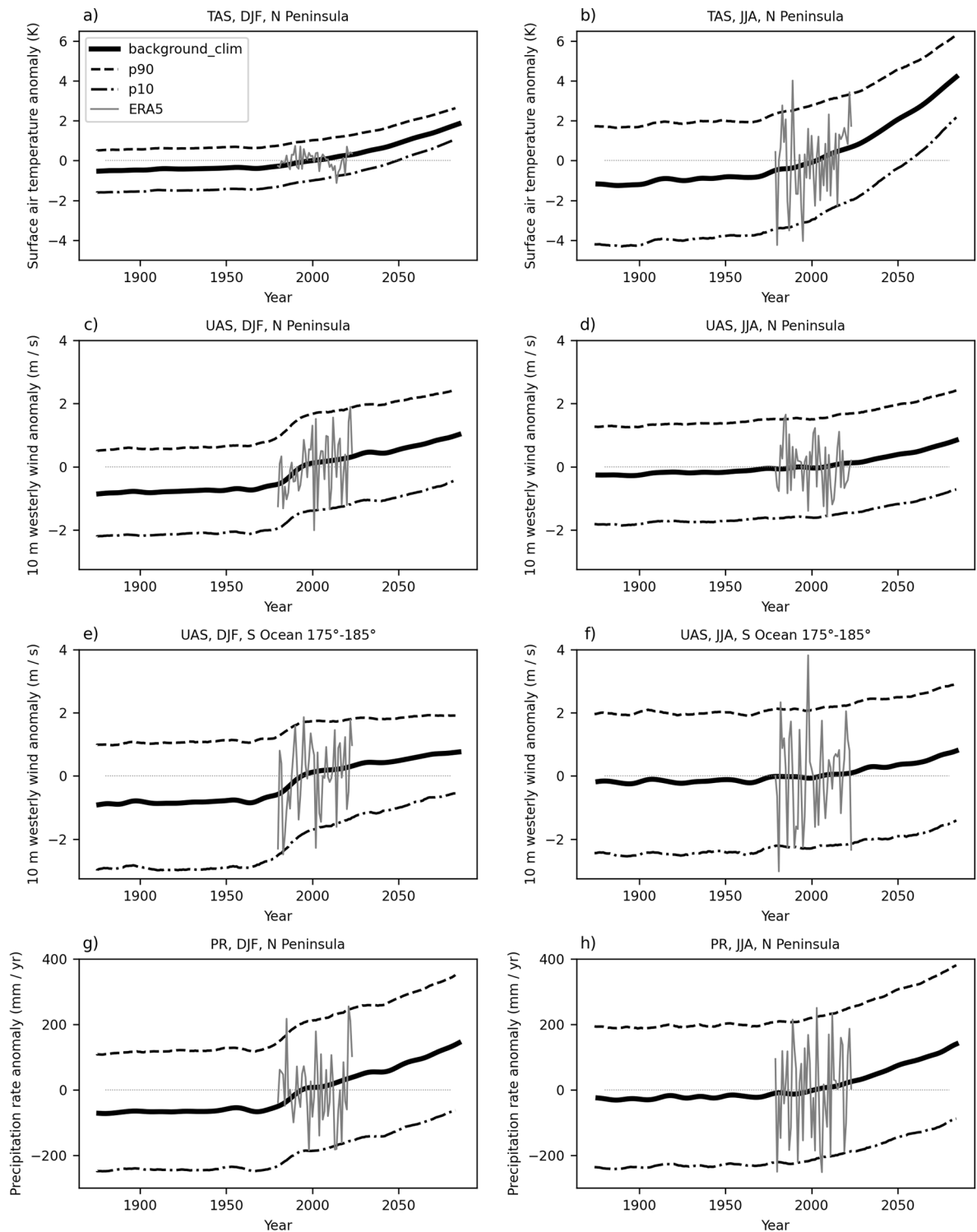
Fig. 4 | Historical and projected background climate, low extremes (p10) and high extremes (p90) at example locations. Time series of multi-model mean summer (DJF) (**a**, **c**, **e**, **g**) and winter (JJA) (**b**, **d**, **f**, **h**) surface-air temperature (**a**, **b**), near-surface (10 m) westerly wind component (**c**–**f**) and precipitation rate (**g**, **h**) in ERA5 (1979–2023) (grey); and CMIP6 background climate (solid line), 10th percentile (dot-dashed line) and 90th percentile (dashed line). The output is displayed as anomalies relative to means over the period of available ERA5 data (1979–2023).

The CMIP6 experiments used were historical up to 2014 and SSP3-7.0 from 2015 to the end of the century. The latest year shown is 2085 due to the temporal smoothing window used for the Lanczos low-pass filter (see Methods section for details). The first, second and fourth rows show spatial averages over the north Peninsula region (shown by the box in Fig. 1); the third row shows spatial averages over a region in the Southern Ocean centred on 180° in longitude (175°E–175°W).
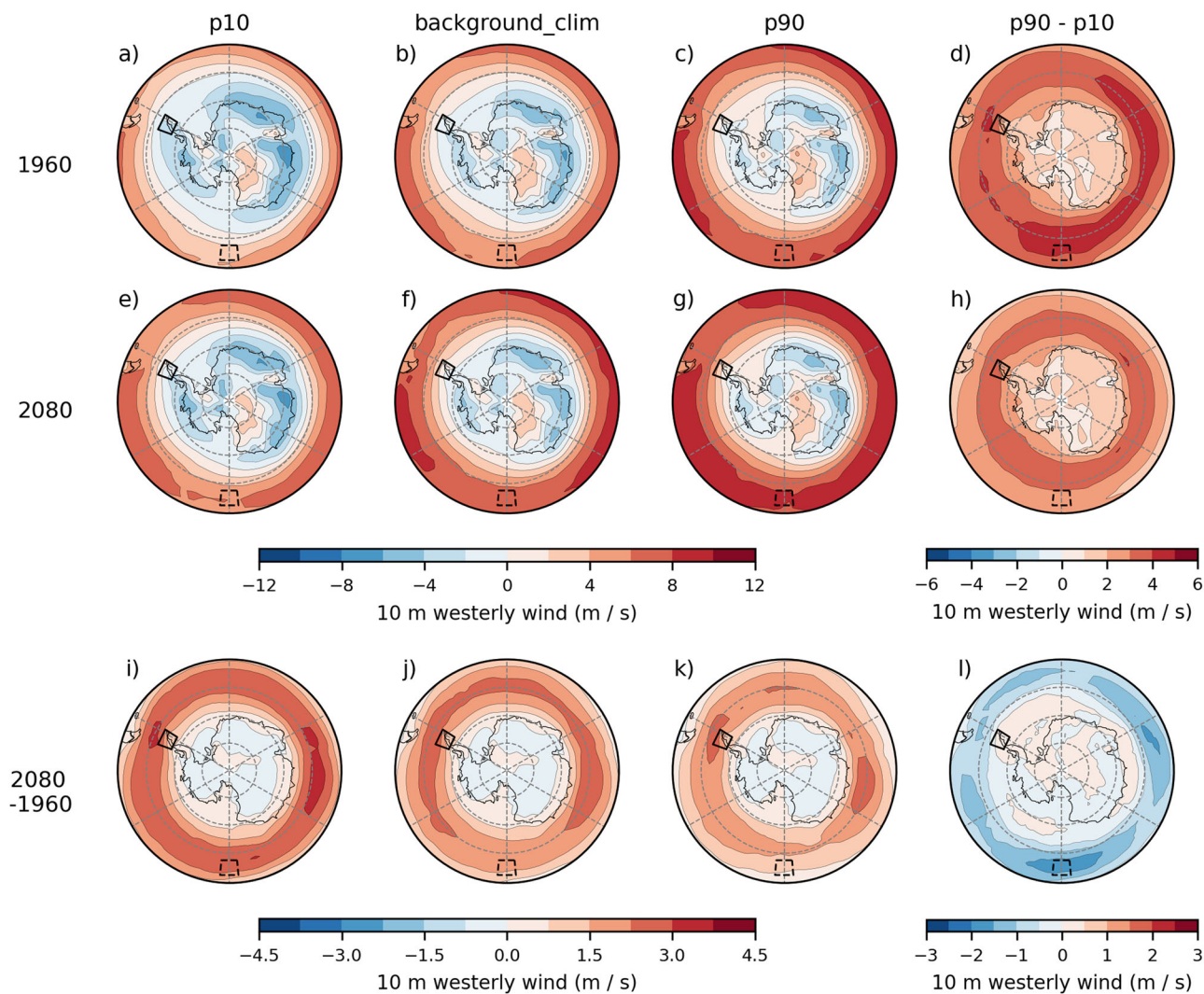
Fig. 5 | CMIP6 multi-model mean summer (DJF) 10 m westerly wind component (UAS) climatologies both pre-ozone hole (1960, from historical runs, top row) and late 21st century (2080, from SSP3-7.0 runs, middle row) and difference between 2080 and 1960 (bottom row). The columns show, from left to right, low extremes (p10) (**a**, **e**, **i**), background mean climate (background_clim) (**b**, **f**, **j**), high extremes (p90) (**c**, **g**, **k**) and the differences between high and low extremes (i.e. the 3rd column minus the first column) (**d**, **h**, **l**). The box with bold black borders shows the location of the north Peninsula region referred to in the main text and used in time series plots in Fig. 4. The box spans the latitudes 62.5°S–67.5°S and longitudes 70°W–57.5°W. The region over the Southern Ocean referred to in the main text is indicated by an additional black box with dashed borders, latitude range 62.5°S–67.5°S and longitude range 175°E–175°W.

(Fig. 7, bottom row). This is consistent with the well-known increases in extreme precipitation events as the moisture-carrying capacity of the atmosphere increases under global warming, with spatial differences associated with regional factors such as dynamical suppression or enhancement[9]. The latter point helps to explain the very different relative changes in PR and TAS extremes in the vicinity of retreating sea ice (i.e. compare Figs. 2 and 8). Two factors of particular relevance here are storm track shifts, exerting a dynamic influence on precipitation extremes (e.g. refs. 19,33), and sea ice retreat, exerting a regional thermodynamic impact (e.g. ref. 13). From a zonal mean perspective (Fig. 8), changes in PR exhibit a clear correspondence to changes in the westerlies seen in UAS, with a distinct single maximum at about 60°S in summer and a broader latitude range of increases and a less clear peak in winter (compare Figs. 6 and 8). However, in terms of extremes, there is not a direct correspondence between UAS and PR, in particular, the distinct narrowing in the range in summer UAS extremes at 55–60°S (e.g. Fig. 6d) is not clearly present in PR (Fig. 8d). There is a local minimum in the PR extremes range at similar latitudes

(~60°S), which is even slightly negative at some longitudes (Fig. 7l), which may be related to the narrowing in the UAS extremes range. At higher latitudes along coastal Antarctica and the Peninsula, at around 60–70°S, high extremes in PR exhibit enhanced increases both in summer and winter (Figs. 7 and 8). Both wider atmospheric warming and increased open ocean area potentially contribute to this, although the relative importance of these factors is difficult to disentangle since precipitation generally occurs away from its moisture sources. Sensitivity studies or moisture tracing capabilities will be important in future studies to isolate specific factors such as sea ice and sea surface temperature change.

The time series of precipitation extracted from ERA5 over the northern Peninsula exhibits seasonal differences that illustrate the strong link to dynamic factors, such as a summer increase during the ozone hole formation period (Fig. 4g, h). The time series plots also illustrate that the forced changes should be set in the context of large inter-annual variability in precipitation and that present-day extreme seasons already span a large proportion of what might be expected in future seasons.
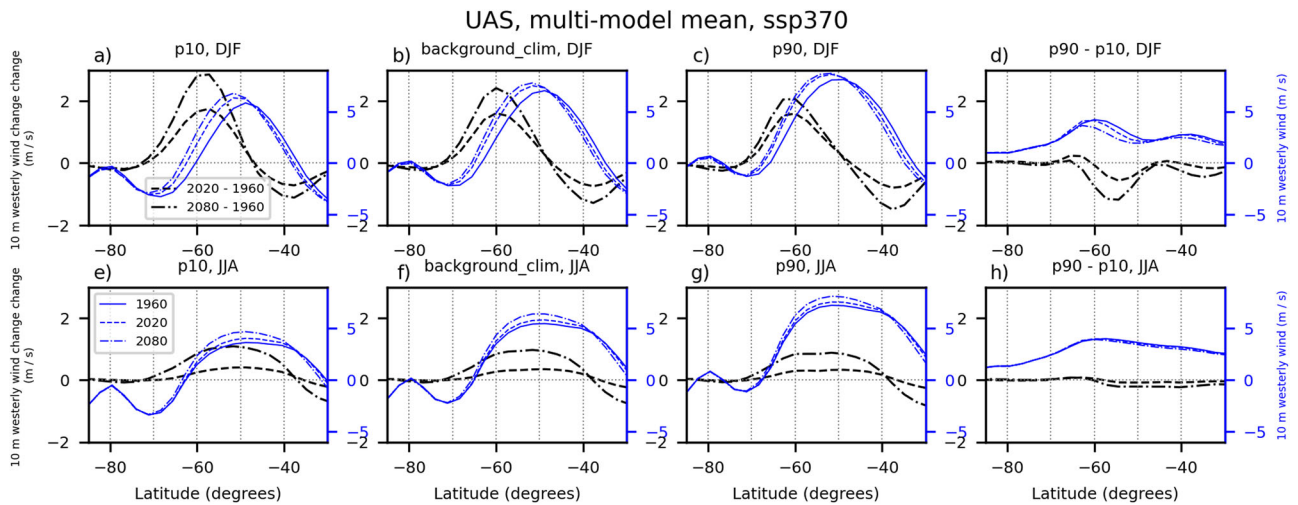
Fig. 6 | CMIP6 multi-model mean zonal mean summer (upper row) and winter (lower row) UAS changes in 2020 and 2080 relative to 1960 (pre-ozone hole). Changes are shown for low extremes (p10) (left column, **a**, **e**), background climate (second colum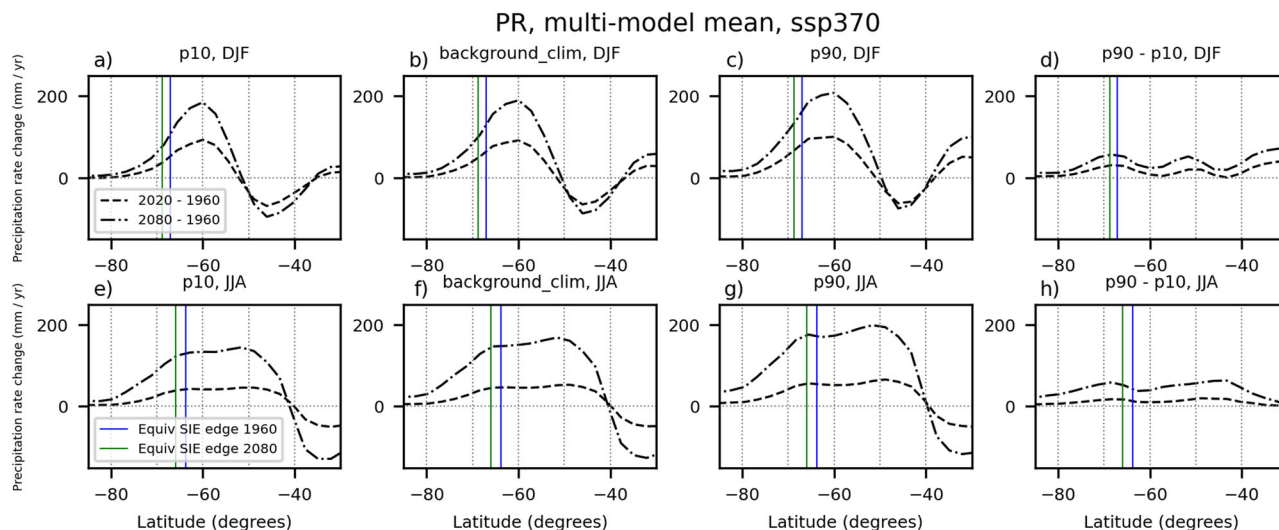n, **b**, **f**), high extremes (third column, **c**, **g**) and the differences between p90 and p10 (right column, **d**, **h**). Climatologies are additionally shown by blue lines in the years 1960, 2020 (present-day) and 2080 (late 21st century), with a different vertical scale indicated on the right of each plot.
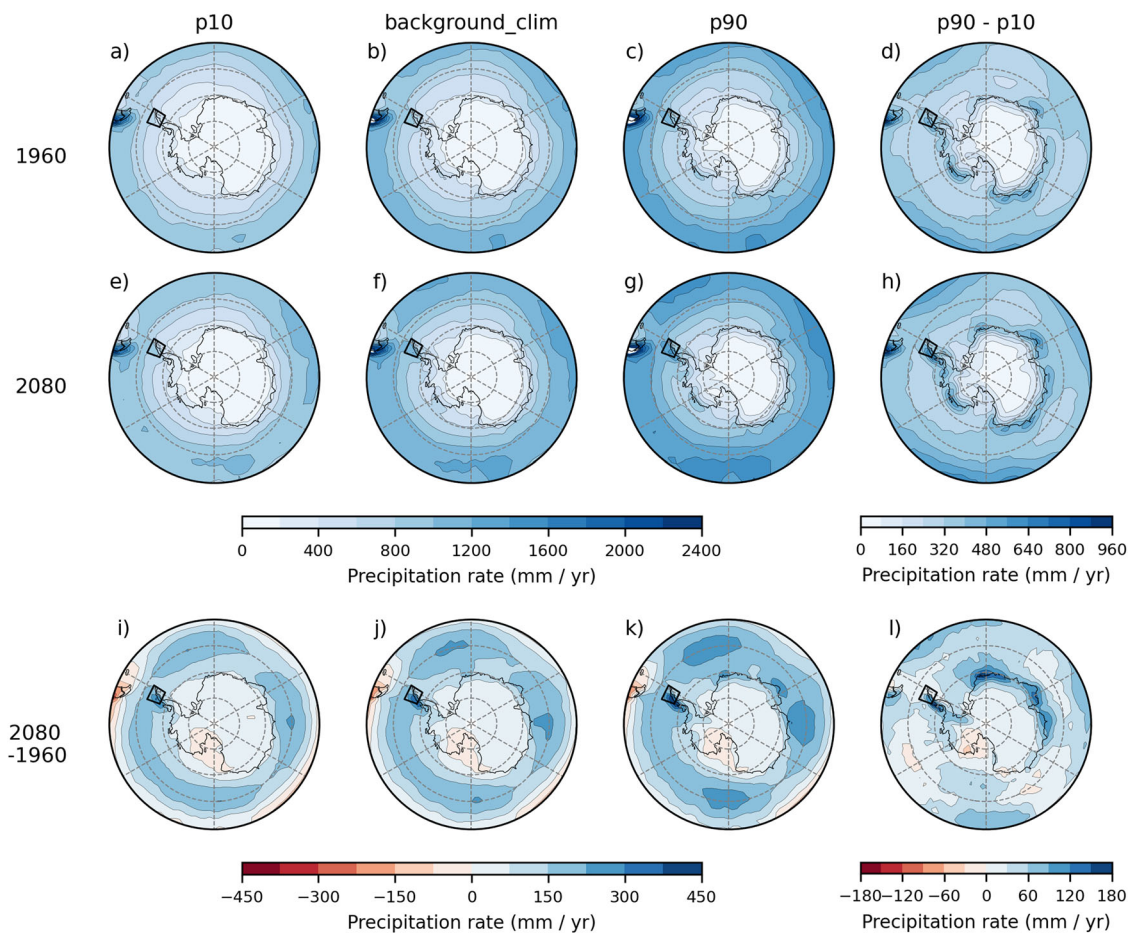
Fig. 7 | CMIP6 multi-model mean summer (DJF) total surface precipitation rate (PR) climatologies both pre-ozone hole (1960, from historical runs, top row) and late 21st century (2080, from SSP3-7.0 runs, middle row) and difference between 2080 and 1960 (bottom row). The columns show, from left to right, low extremes (p10) (**a**, **e**, **i**), background mean climate (background_clim) (**b**, **f**, **j**), high extremes (p90) (**c**, **g**, **k**) and the differences between high and low extremes (i.e. the 3rd column minus the first column) (**d**, **h**, **l**). Note that the colour bar has been swapped compared to figures showing maps of other variables TAS and UAS, with blue showing larger values. The box with bold black borders shows the location of the north Peninsula region referred to in the main text and used in time series plots in Fig. 4.

Fig. 8 | CMIP6 multi-model mean zonal mean summer (upper row) and winter (lower row) PR changes in 2020 and 2080 relative to 1960 (pre-ozone hole). Changes are shown for low extremes (p10) (left column, **a**, **e**), background climate (second column, **b**, **f**), high extremes (third column, **c**, **g**) and the differences between p90 and p10 (right column, **d**, **h**). Climatologies of the multi-model mean equivalent latitudes (see Methods) of the sea ice edge are shown, centred on the years 1960 (blue vertical lines) and 2080 (green vertical lines).

Discussion

This paper provides the first multi-variate overview of the response of Antarctic extreme seasons to climate forcing over the 20th and 21st centuries, with a particular focus on the period between 1960 and 2080, during which both greenhouse gases and stratospheric ozone concentrations have been, and are projected to be, important climate forcings. The main question addressed in this study is the degree to which changes in extremes correspond to changes in background climate in surface air temperature (TAS), near-surface zonal wind (UAS) and total surface precipitation rate (PR). The analysis is based on large ensemble simulations from five different CMIP6 climate models, which together provide approximately 200 different realisations and, therefore, allow an examination of changes in extreme seasons. The main conclusions are as follows:

1. Externally forced changes in extreme seasons do not in general follow changes in background climate. The characteristics of these differences vary considerably across near-surface temperature, near-surface westerly wind and precipitation rate and between summer and winter.
2. For surface air temperature (TAS), the main differences between changes in extremes and background climate occur in the winter season, likely associated with sea ice retreat reducing the frequency of extreme cold years.
3. For westerly near-surface wind (UAS), the results are consistent with a strong link to changes in the westerly jet/storm track. A maximum in UAS variability on the poleward flank of the jet moves with the jet under climate change resulting in asymmetric changes in high and low extremes.
4. For precipitation rate (PR) there is generally a slightly stronger increase in high extremes compared to background climate change and low extremes, with a strong link to jet structure and a possible link to sea ice retreat.

Model sensitivity of these conclusions was assessed and they were found to be remarkably qualitatively robust across the individual LE models. To show this, single-model versions of the multi-model mean zonal mean plots shown in Figs. 2, 6 and 8 are available in Figs. S4–S19 of the Supplementary Material.

- For Conclusion 2, as shown in Fig. S1, the lack of sea ice in MIROC6 is consistent with the lack of narrowing in the p90–p10 range in winter, which is seen in all the other LE models (compare panel h of Figs. S4–S8).

- For Conclusion 3, the zonal mean profiles of change in UAS are qualitatively consistent across the five LE models with poleward shifts in maxima of UAS variability on the poleward flank of the jet in summer (see panels d of Figs. S9–S13). Indeed, all five models do a reasonable job of capturing the summer zonal mean jet structure with no outliers compared to the rest of the CMIP6 ensemble (see Table S1). The small differences between changes in p10 and p90 in winter (JJA) are consistent across all the models.

- For Conclusion 4 the slightly stronger increase in high PR extremes (p90) is a robust feature across the models (panels d of Figs. S14–S18), although it is noticeably weaker at high latitudes for MIROC6 and MPI-ESM1-2-LR in both winter and summer (Figs. S16 and S17). However, it is notable that both models exhibit negative sea ice biases in their historical simulations, which reduces the capacity for future increases in high-latitude open ocean areas and associated increases in moisture availability. In addition, both models are outliers in terms of winter jet latitude with large equatorward jet biases (Table S2), potentially resulting in weaker interactions between poleward shifting storm tracks and the Antarctic coastline. However, cause and effect are difficult to determine in this case as the jet latitude and sea ice biases are likely related.

Many other factors potentially play a role in inter-model differences in simulated changes, such as the representation of clouds, or global climate sensitivity. A relevant example of this is that the UKESM1-0-LL is the only one of the five LE models that includes interactive ozone chemistry[34]. It has been found that, in general, models with interactive ozone chemistry exhibit larger stratospheric ozone loss and recovery along with more pronounced associated effects[34]. This may help to explain why, in Fig. S13, the summer-season westerlies in UKESM1-0-LL exhibit almost no change between 2020 and 2080, a period when stratospheric ozone recovery is acting to weaken the summer westerlies, whereas greenhouse gas forcing is acting to strengthen them. In the other four models westerlies generally strengthen over the same period, consistent with a weaker ozone recovery effect (Figs. S9–S12). Overall, a key message is that the above conclusions are robust to the exclusion of the models with large biases in sea ice and westerly jets and, indeed quantitatively, strengthened (Figs. S17–S19). More detailed consideration of model performance in these aspects will be key in the planned future downscaling of LE datasets for more detailed assessments of trends and variability in extreme events.

Table 1 | CMIP6 models included, with grids and number of realisations

Model name	Atmospheric grid	Number of realisations	Realisation IDs
ACCESS-ESM1-5	~1.9° × 1.3°	40	r[1–40]i1p1f1
CanESM5	~2.8° × 2.8°	50	r[1–25]i1p1pf1, r[1–25]i1p2f1
MIROC6	~1.4° × 1.4°	50	r[1–50]i1p1f1
MPI-ESM1-2-LR	~1.9° × 1.3°	30	r[1–30]i1p1f1
UKESM1-0-LL	~1.9° × 1.2°	14	r[1–4,8–13,16–19]i1p1f2

In terms of wider implications, an important concept relevant to impacts is the magnitude of changes in background climate relative to the range of conditions seen in the historical period (i.e. the 10th–90th percentile range). This is related to the concepts of 'signal to noise' and 'time of emergence', which are used in the detection of climate signals and as measures of their significance (e.g. ref. 35) Extreme seasons that are a larger departure from historical experience are more likely to put a strain on natural systems (e.g. animal populations or ice shelves) and human infrastructure. Of the three variables assessed here, temperature exhibits the strongest change relative to the historical variability, especially in summer (Fig. 4). For UAS and PR, the changes in background climate are less pronounced compared to historical variability, especially in winter. The main implication of this is that significant extreme summer TAS, and the associated impacts on sea level (through ice shelf weakening/breakup) and regional ecosystems (e.g. through snow-to-rain transition), will emerge sooner than for PR and UAS. Possibly of greatest relevance to the global climate system is the projected reduction in summer UAS variability on the poleward flank of the westerly jet (i.e. the negative changes in UAS_{p90}–UAS_{p10} between 55 and 60°S apparent in, for example, Figs. 5l and 6d), since wind variability is known to be an important driver of variability in the Southern Ocean carbon sink[36]. Further research would be required to quantify any such impact.

Of further relevance to impacts, a priority for future research is to assess trends in sub-seasonal extremes and better understand links between specific extreme weather events and extreme seasons. For example, an extreme season caused by consistent anomalies (i.e. not extreme individual weather events) will have different impacts from an extreme season driven by a small number of individual extreme weather events. A particular example is that annual and seasonal surface precipitation totals comprise a large contribution from a small number of extreme precipitation events, particularly in near-coastal regions[37]. In addition to the broad-scale shifting and strengthening of storm tracks and changes in sea ice, other factors that will be important to consider in understanding the behaviour of Antarctic extreme events include linkages between anomalies in the stratosphere and the surface (e.g. the strong stratospheric anomalies seen during the March 2022 heatwave[38]), increasing precipitation intensity associated with extra-tropical cyclones[39] and the role of drivers from lower latitudes towards the tropics[40]. A key challenge in considering such factors is that model configurations used for LEs are generally necessarily low resolution, leading to a requirement for downscaling approaches for extracting impacts-relevant information from LEs.

There are also dynamic questions that emerge from the assessment of extreme seasons presented here. Why, for example, is there such a large contrast between summer and winter in terms of variability on the poleward side of the time-mean jet? Possible factors include (i) cyclonic wave-breaking (CWB), which is much stronger in austral summer than in winter[41] and exhibits distinct changes under forcing[17] and (ii) seasonal contrasts in the strength of atmospheric eddy feedbacks[18]. Further research on these questions is a priority for understanding dynamical linkages from the surface, through the troposphere and above. Other mechanisms of potential importance for understanding divergence between changes in extremes and background climate are large-scale factors such as tropical teleconnections[42] and small-scale local drivers such as foehn warming[15,43].

This study highlights two elements of the climate system that have a major influence on Antarctic extremes and are, therefore, key in terms of evaluating models to be used in the study of Antarctic extreme events. They are (i) sea ice cover, which most directly affects TAS, and (ii) the westerly jet, which is of clear relevance for UAS and PR. With regard to the westerly jet, we show that it is important to go beyond widely used indices of time-mean zonal-mean latitude and speed but to also consider variability and its latitudinal/spatial structure. Looking beyond extreme seasons, the westerlies are also of particular relevance for small-scale local processes affecting TAS, such as foehn winds, which are sensitive to large-scale drivers but can only be captured using high-resolution modelling or dynamical downscaling.

Methods
Climate model and reanalysis data
Here we use the CMIP6 dataset[21] to provide simulated evolutions of extreme seasons over the 20th and 21st centuries. The focus is on seasonal means, for example, time series of austral summer-mean surface air temperature. Summer (December–February; DJF) and winter (June–August; JJA) means are calculated from monthly means of four variables: surface air temperature at 2 m (CMIP6 variable name 'tas', referred to as TAS in this manuscript), zonal wind at 10 m ('uas', UAS), total surface precipitation rate ('pr', PR) and sea ice concentration ('siconc'). A subset of CMIP6 models with large ensembles of simulations was selected (see Table 1), as these provide large sample sizes for assessing the statistical distribution of extreme seasons. In CMIP6 terminology, repeated simulations of a given model with the same external forcing experiment (e.g. the same future scenario forcing) are referred to as realisations. Models with large ensembles of simulations are those with a large number of realisations for one or more forcing experiments. In this study, the focus is on simulations from historical and SSP3-7.0 ScenarioMIP forcing experiments.

A sea ice equivalent latitude method[26,44] was used to calculate an equivalent latitude from the sum of sea ice extent (SIE) and the area of the Antarctic continent, by conceptualising the latitude to which sea ice would extend if it was zonally symmetric. The area of the Antarctic continent in each model was calculated as the difference of earth surface area south of 60°S and the ocean area south of 60°S calculated from CMIP6 variable 'areacello'. Monthly SIE, for the first ensemble realisation only, was calculated on the model native grid from sea ice concentration (CMIP6 variable siconc), and then the equivalent latitude was calculated from the SIE climatology for the relevant 31-year period. Only the first realisation was required since no analysis of extreme seasons in sea ice was conducted and climatological-mean circumpolar averages do not vary significantly across different realisations of a given model experiment. Finally, the multimodel mean was taken. An ice-free Antarctic (SIE of 0) would correspond to an equivalent latitude of ~71°S.

To combine gridded data from different models, which is necessary for plotting spatial maps, a linear interpolation re-gridding method was used to interpolate onto a common grid. The common grid chosen was used for the CanESM5, which is the lowest resolution of the models used (Table 1). The regional spatial averages were used to help provide comparable diagnostics between CMIP6 and ERA5 data. In particular the greater granularity of ERA5 is averaged over the defined regions. Although point observation measurements are available over the Peninsula, they are not suitable for comparisons with low-resolution gridded output, which represents average conditions over multiple environments from marine to terrestrial rather than at a specific locality which is dependent on specific local factors.

Fig. 9 | An example time series to illustrate the methodology for extracting background climate and extreme seasons from the CMIP6 ensemble. Simulated winter (JJA) mean surface air temperature time series at the location of Vernadsky research station (65.2°S, 64.3°W) from the CanESM5 model. **a** The first realisation (blue dash-dot line) following the historical and SSP3-7.0 forcing scenarios. The thin grey lines show all the other 49 realisations with realisation mean shown as the thick grey line. The smoothed realisation mean is given by the thick black line and the upper (90th) and lower (10th) percentiles shown by the thick black dashed and dash-dot lines. In (**b**), the same smoothed realisation means are shown, but the individual realisations (grey) are shown only in relation to calculating p10(1960) and p10(2080) from Eq. (3). The vertical blue and red lines show the 10th and 90th percentiles of the 1550 residuals for each of the two 31-year windows shown.
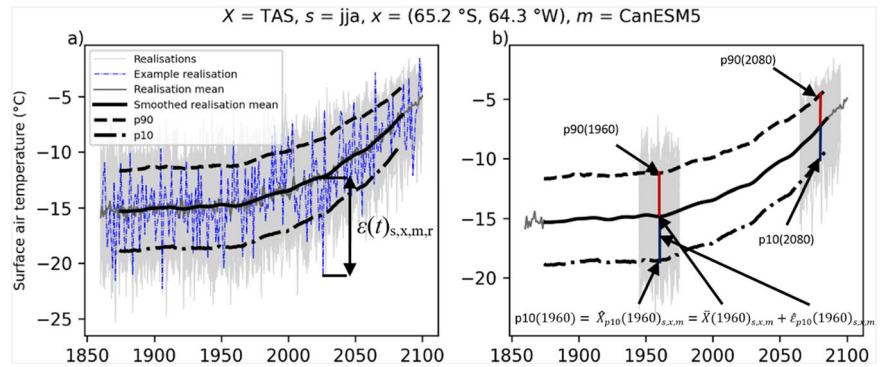
Reanalysis data from the European Centre for Medium-Range Weather Forecasts (ECMWF) ERA5 dataset[45] was used to provide comparisons between the output from the many realisations simulated by the CMIP6 climate models and the evolution of key variables constrained by observations of the actual realisation of the real world. For comparison with the CMIP6 model output, the same monthly mean variables of surface air temperature, near-surface westerly wind and total surface precipitation rate were used.

Analysis of seasonal extremes in model simulations

The starting point for describing the approach used to calculate seasonal extremes in the CMIP6 model output is a time series of seasonal mean values for all years in the range 1850 through 2100 where matching historical and SSP experiments (i.e. those with the same realisation number representing effectively the same continuous simulation) are joined together. An example for a specific location is shown by the blue dash-dot line in Fig. 9a.

For each season (s), grid location (x), model (m) and realisation (r) the time series of a climate variable X (e.g. the blue line in Fig. 9a) can be expressed as

$$X(t)_{s,x,m,r} = \bar{X}(t)_{s,x,m} + \varepsilon(t)_{s,x,m,r} \qquad (1)$$

where ε denotes residuals about the estimated background climate state (indicated by the overbar). For each model, this is calculated by taking a realisation mean (i.e. mean over all realisations) and then applying a low-pass filter as follows.

$$\bar{X}(t)_{s,x,m} = L\left(\frac{1}{n}\sum_{r=0}^{n-1} X(t)_{s,x,m,r}\right) \qquad (2)$$

The Lanczos low-pass filter (L) was applied using a moving window of width 31 with weights giving a cut-off period of 20 years. The results were not found to be significantly affected by reducing the cut-off period to 10 or 5 years (not shown). In principle, the low-pass filter would not be required with a large enough ensemble of realisations, however, it was found that for the intra-model ensemble sizes available here (10–20 for some of the models used), some short-term variability was still present in the realisation means without application of the filter (e.g. see bold solid dark grey line in Fig. 9a).

Thresholds for extreme conditions are defined relative to the background mean climate. For each model, the 10th and 90th percentiles of residuals, ε, across multiple realisations are used to define low and high extremes. To capture potential changes in variability over time, a moving window approach is used whereby the percentiles are drawn from a sample

over the interval $t-15$ years to $t+15$ years (i.e. a 31-year window). Figure 9b illustrates the sampling approach for years 1960 and 2080, with the 10th–90th percentile range shown by the vertical blue and red lines, respectively. For this example, the CanESM5 model has 50 ensemble members, therefore for each year the sample of residuals is 1550 in size. For a given percentile, e.g. p90, this is expressed as

$$\hat{X}_{p90}(t)_{s,x,m} = \bar{X}(t)_{s,x,m} + \hat{\varepsilon}_{p90}(t)_{s,x,m} \qquad (3)$$

where the hat denotes the moving window sample shown in Fig. 9b. Figure 9 shows the time series from just one model. Multi-model means of the background climate $\bar{X}(t)_{s,x}$, low extremes $\hat{X}_{p10}(t)_{s,x}$ and high extremes $\hat{X}_{p90}(t)_{s,x}$ are calculated as unweighted means across models m. For simplicity, these quantities are referred to in the text as 'background climate', 'p10' and 'p90', respectively.

Data availability

The data that support the findings of this study are openly available. CMIP6 data can be accessed at https://esgf-index1.ceda.ac.uk/search/cmip6-ceda/. ERA5 data is available to researchers, with details on access at https://www.ecmwf.int/en/forecasts/dataset/ecmwf-reanalysis-v5.

Code availability

The underlying code for this study is not publicly available but may be made available to qualified researchers on reasonable request from the corresponding author.

References

1. Chown, S. L. et al. *Antarctic Climate Change and the Environment: A Decadal Synopsis and Recommendations for Action* (Scientific Committee on Antarctic Research, Cambridge, UK, 2022).
2. Bracegirdle, T. J. et al. Twenty first century changes in Antarctic and Southern Ocean surface climate in CMIP6. *Atmos. Sci. Lett.* **21**, e984 (2020).
3. Holmes, C. R., Bracegirdle, T. J. & Holland, P. R. Antarctic sea ice projections constrained by historical ice cover and future global temperature change. *Geophys. Res. Lett.* **49**, e2021GL097413 (2022).
4. Scambos, T., Hulbe, C. & Fahnestock, M. Climate-induced ice shelf disintegration in the Antarctic Peninsula. In *Antarctic Peninsula Climate Variability: Historical and Paleoenvironmental Perspectives* [eds E. Domack, A. Levente, A. Burnet, R. Bindschadler, P. Convey

and M. Kirby] 79–92 (Cambridge University Press, Cambridge, UK, 2003).

5. van Wessem, J. M., van den Broeke, M. R., Wouters, B. & Lhermitte, S. Variable temperature thresholds of melt pond formation on Antarctic ice shelves. *Nat.Clim. Chang.* **13**, 161–166 (2023).

6. Scambos, T. A., Bohlander, J. A., Shuman, C. A., & Skvarca, P. Glacier acceleration and thinning after ice shelf collapse in the Larsen B embayment, Antarctica. *Geophys. Res. Lett.* **31**, L18402 (2004).

7. Fretwell, P. T., Boutet, A. & Ratcliffe, N. Record low 2022 Antarctic sea ice led to catastrophic breeding failure of emperor penguins. *Commun. Earth Environ.* **4**, 273 (2023).

8. Siegert, M. J. et al. Antarctic extreme events. *Front. Environ. Sci.* **11**, 1229283 (2023).

9. Seneviratne, S. I., et al. Weather and climate extreme events in a changing climate. In *Climate Change 2021: The Physical Science Basis. Contribution of Working Group I to the Sixth Assessment Report of the Intergovernmental Panel on Climate Change* [Masson-Delmotte, V., P. Zhai, A. Pirani, S.L. Connors, C. Péan, S. Berger, N. Caud, Y. Chen, L. Goldfarb, M.I. Gomis, M. Huang, K. Leitzell, E. Lonnoy, J.B.R. Matthews, T.K. Maycock, T. Waterfield, O. Yelekçi, R. Yu, & B. Zhou (eds.)] 1513–1766 (Cambridge University Press, Cambridge, UK, 2021).

10. Tamarin-Brodsky, T., Hodges, K., Hoskins, B. J. & Shepherd, T. G. A dynamical perspective on atmospheric temperature variability and its response to climate change. *J. Clim.* **32**, 1707–1724 (2019).

11. Holmes, C. R., Woollings, T., Hawkins, E. & de Vries, H. Robust future changes in temperature variability under greenhouse gas forcing and the relationship with thermal advection. *J. Clim.* **29**, 2221–2236 (2016).

12. Olonscheck, D., Schurer, A. P., Lucke, L. & Hegerl, G. C. Large-scale emergence of regional changes in year-to-year temperature variability by the end of the 21(st) century. *Nat. Commun.* **12**, 7237 (2021).

13. Hartmuth, K., Papritz, L., Boettcher, M. & Wernli, H. Arctic seasonal variability and extremes, and the role of weather systems in a changing climate. *Geophysi. Res. Lett.* **50**, (2023).

14. Turner, J., Maksym, T., Phillips, T., Marshall, G. J. & Meredith, M. P. The impact of changes in sea ice advance on the large winter warming on the western Antarctic Peninsula. *Int. J. Climatol.* **33**, 852–861 (2013).

15. Lu, H. et al. Extreme warm events in the South Orkney Islands, Southern Ocean: compounding influence of atmospheric rivers and föhn conditions. *Q. J. R. Meteorol. Soc.* **149**, 3645–3668 (2023).

16. Schneider, T., Bischoff, T. & Plotka, H. Physics of changes in synoptic midlatitude temperature variability. *J. Clim.* **28**, 2312–2331 (2015).

17. Barnes, E. A. & Polvani, L. Response of the midlatitude jets, and of their variability, to increased greenhouse gases in the CMIP5 models. *J. Clim.* **26**, 7117–7135 (2013).

18. Simpson, I. R. & Polvani, L. M. Revisiting the relationship between jet position, forced response, and annular mode variability in the southern midlatitudes. *Geophys. Res. Lett.* **43**, 2896–2903 (2016).

19. Lenaerts, J. T. M., Fyke, J. & Medley, B. The signature of ozone depletion in recent antarctic precipitation change: a study with the community earth system model. *Geophys. Res. Lett.* **45**, 12931–12939 (2018).

20. Lockwood, J. F. et al. Seasonal prediction of UK mean and extreme winds. *Q. J. R. Meteorol. Soc.* **149**, 3477–3489 (2023).

21. Eyring, V. et al. Overview of the Coupled Model Intercomparison Project Phase 6 (CMIP6) experimental design and organization. *Geosci. Model Dev.* **9**, 1937–1958 (2016).

22. Bracegirdle, T. J., Connolley, W. M. & Turner, J. Antarctic climate change over the twenty first century. *J. Geophys. Res.-Atmos.* **113**, https://doi.org/10.1029/2007jd008933 (2008).

23. Bracegirdle, T. J., Stephenson, D. B., Turner, J. & Phillips, T. The importance of sea ice area biases in 21st century multimodel projections of Antarctic temperature and precipitation. *Geophys. Res. Lett.* **42**, 10,832–10,839 (2015).

24. Davy, R. & Griewank, P. Arctic amplification has already peaked. *Environ. Res. Lett.* **18**, 084003 (2023).

25. Swart, N. C., Fyfe, J. C., Gillett, N. & Marshall, G. J. Comparing trends in the southern annular mode and surface westerly jet. *J. Clim.* **28**, 8840–8859 (2015).

26. Bracegirdle, T. J., Hyder, P. & Holmes, C. R. CMIP5 diversity in southern westerly jet projections related to historical sea ice area; strong link to strengthening and weak link to shift. *J. Clim.* **31**, 195–211 (2018).

27. Orr, A. et al. Is our dynamical understanding of the circulation changes associated with the Antarctic ozone hole sensitive to the choice of reanalysis dataset? *Atmos. Chem. Phys.* **21**, 7451–7472 (2021).

28. Bracegirdle, T. J. et al. Assessment of surface winds over the Atlantic, Indian, and Pacific Ocean sectors of the Southern Ocean in CMIP5 models: historical bias, forcing response, and state dependence. *J. Geophys. Res.- Atmos.* **118**, 547–562 (2013).

29. Simpson, I. R., Shaw, T. A. & Seager, R. A diagnosis of the seasonally and longitudinally varying midlatitude circulation response to global warming. *J. Atmos. Sci.* **71**, 2489–2515 (2014).

30. Chen, G. & Held, I. M. Phase speed spectra and the recent poleward shift of Southern Hemisphere surface westerlies. *Geophys. Res. Lett.* **34**, L21805 (2007).

31. Butler, A. H., Thompson, D. W. J & Heikes, R. The steady-state atmospheric circulation response to climate change-like thermal forcings in a simple general circulation model. *J. Clim.* **23**, 3474–3496 (2010).

32. Chemke, R. The future poleward shift of Southern Hemisphere summer mid-latitude storm tracks stems from ocean coupling. *Nat. Commun.* **13**, 1730 (2022).

33. Shaw, T. A. et al. Storm track processes and the opposing influences of climate change. *Nat. Geosci.* **9**, 656–664 (2016).

34. Revell, L. E., Robertson, F., Douglas, H., Morgenstern, O. & Frame, D. Influence of ozone forcing on 21st century Southern Hemisphere surface westerlies in CMIP6 models. *Geophys. Res. Lett.* **49**, e2022GL098252 (2022).

35. Hawkins, E. & Sutton, R. Time of emergence of climate signals. *Geophys. Res. Lett.* **39**, L01702 (2012).

36. Keppler, L. & Landschutzer, P. Regional wind variability modulates the Southern Ocean carbon sink. *Sci. Rep.* **9**, 7384 (2019).

37. Turner, J. et al. The dominant role of extreme precipitation events in Antarctic snowfall variability. *Geophys. Res. Lett.* **46**, 3502–3511 (2019).

38. Blanchard-Wrigglesworth, E., Cox, T., Espinosa, Z. I. & Donohoe, A. The largest ever recorded heatwave—characteristics and attribution of the Antarctic heatwave of March 2022. *Geophys. Res. Lett.* **50**, e2023GL104910 (2023).

39. Catto, J. L. et al. The future of midlatitude cyclones. *Curr. Clim. Change Rep.* **5**, 407–420 (2019).

40. Wille, J. D. et al. The extraordinary March 2022 east Antarctica "heat" wave. Part I: observations and meteorological drivers. *J. Clim.* **37**, 757–778 (2024).

41. Song, J., Li, C. Y., Pan, J. & Zhou, W. Climatology of anticyclonic and cyclonic Rossby wave breaking on the dynamical tropopause in the Southern Hemisphere. *J. Clim.* **24**, 1239–1251 (2011).

42. Clem, K. R. et al. Record warming at the South Pole during the past three decades. *Nat. Clim. Change* **10**, 762–770 (2020).

43. Gilbert, E., Orr, A., King, J. C., Renfrew, I. A. & Lachlan-Cope, T. A 20-year study of melt processes over Larsen C ice shelf using a high-resolution regional atmospheric model: 1. model configuration and validation. *J. Geophys. Res.-Atmos.* **127**, e2021JD034766 (2022).

44. Eisenman, I. Geographic muting of changes in the Arctic sea ice cover. *Geophys. Res. Lett.* **37**, L16501 (2010).

45. Hersbach, H. et al. The ERA5 global reanalysis. *Q. J. R. Meteorol. Soc.* **146**, 1999–2049 (2020).

Acknowledgements

Author contributions

Competing interests

The authors declare no competing interests.

Additional information

Supplementary information The online version contains supplementary material available at https://doi.org/10.1038/s41612-024-00822-y.

Correspondence and requests for materials should be addressed to Thomas J. Bracegirdle.

Reprints and permissions information is available at http://www.nature.com/reprints

Publisher's note Springer Nature remains neutral with regard to jurisdictional claims in published maps and institutional affiliations.